

1 Revision 1

2 **Decompression experiments for sulfur-bearing**  
3 **hydrous rhyolite magma: Redox evolution during**  
4 **magma decompression**

5  
6  
7  
8 Satoshi Okumura<sup>1\*</sup>, Hidemi Ishibashi<sup>2</sup>, Shoichi Itoh<sup>3</sup>, Akimasa Suzumura<sup>3</sup>,  
9 Yoshihiro Furukawa<sup>1</sup>, Takahiro Miwa<sup>4</sup>, and Hiroyuki Kagi<sup>5</sup>

10  
11  
12  
13 <sup>1</sup> Division of Earth and Planetary Materials Science, Department of Earth Science,  
14 Graduate School of Science, Tohoku University, 6-3 Aoba, Aramaki-aza, Aoba, Sendai  
15 980-8578 Miyagi, Japan

16 <sup>2</sup> Department of Geosciences, Faculty of Science, Shizuoka University, 836 Ohya,  
17 Suruga-ku, Shizuoka 422-8529, Japan

18 <sup>3</sup> Division of Earth and Planetary Sciences, Graduate School of Science, Kyoto  
19 University, Kitashirakawa Oiwake-cho, Sakyo-ku, Kyoto 606-8502, Japan

20 <sup>4</sup> National Research Institute for Earth Science and Disaster Resilience, Tennodai 3-1,  
21 Tsukuba, Ibaraki 305-0006, Japan

22 <sup>5</sup> Geochemical Research Center, Graduate School of Science, The University of Tokyo,  
23 7-3-1 Hongo, Bunkyo-ku, Tokyo 113-0033, Japan

24  
25 \*Corresponding author

26 Satoshi Okumura

27 Division of Earth and Planetary Materials Science, Department of Earth Science,  
28 Graduate School of Science, Tohoku University, 6-3 Aoba, Aramaki-aza, Aoba, Sendai  
29 980-8578 Miyagi, Japan.

30 Tel&Fax +81-22-795-7764: Email [satoshi.okumura.d2@tohoku.ac.jp](mailto:satoshi.okumura.d2@tohoku.ac.jp)

33 **Abstract**

34 We performed decompression experiments on sulfur-bearing hydrous rhyolite magma at  
35 a temperature of 800 °C to investigate redox evolution during magma decompression.  
36 The magma was continuously decompressed from 100 MPa to 10–50 MPa at rates of 10  
37 and 100 MPa h<sup>-1</sup>. The evolution of the ferric to total iron ratio (Fe<sup>3+</sup>/Fe<sub>total</sub>) during  
38 decompression was investigated using XANES, and redox evolution was determined  
39 based on a thermodynamic calculation and measured Fe<sup>3+</sup>/Fe<sub>total</sub>. Before decompression,  
40 the sample was buffered from NNO to NNO+1, and the pre-exsolved fluid phase and  
41 sulfide crystal coexisted. Sulfide crystals were found in all decompressed samples, and  
42 Fe<sup>3+</sup>/Fe<sub>total</sub> showed a slight decrease with decompression. It was confirmed that the  
43 sample in a gold capsule was not influenced by the change in redox conditions outside  
44 of the capsule for the timescale of the decompression experiments; thus, the  
45 decompressed sample reflected the redox evolution in magma during decompression.

46 Our experiments indicated that magma decompression causes a slight reduction  
47 when it includes water and sulfur. This evolution is qualitatively explained by sulfur  
48 degassing and fluid-melt redox equilibria. During the fluid-melt redox equilibria,  
49 magma is reduced if the existence of a pre-exsolved fluid phase is assumed, while the  
50 model calculation shows that magma is oxidized when it contains only water or no  
51 pre-exsolved fluid phases. This is because sulfur buffers the oxidation of magma  
52 through a reaction with oxygen in the fluid phase. Therefore, we inferred that the redox  
53 condition of magma is not oxidized during explosive volcanism with a pre-exsolved  
54 fluid phase and closed-system degassing. In contrast, if magma experiences  
55 open-system degassing, it may be oxidized, resulting in the breakdown of sulfide  
56 crystals as observed in some pyroclasts and lavas.

57 **Keywords:** rhyolitic magma, decompression, redox evolution, sulfur, water

58

## 59 INTRODUCTION

60 Water and sulfur are the major volatile components in magma, along with  
61 carbon, chlorine, and fluorine (e.g., Wallace, 2005; Wallace et al., 2015). During the  
62 ascent of magma to the surface (decompression) in volcanic eruptions, these volatiles  
63 show complicated degassing behavior. In particular, water and sulfur dissolve as at least  
64 two chemical species in silicate melt and react with each other in the fluid phase, and  
65 their degassing during the ascent controls redox evolution of magma (Burgisser and  
66 Scaillet, 2007; Blundy et al., 2008; Moussallam et al., 2014; Humphreys et al., 2015).  
67 Investigating the processes of the redox evolution caused by water and sulfur degassing  
68 is essential to the understanding of the oxygen fugacity of magma and the mantle based  
69 on the petrological analysis of groundmass glass in pyroclasts and lavas (e.g.,  
70 Carmichael, 1991; Carmichael and Ghiorso, 1990; Kelley and Cottrell, 2009;  
71 Moussallam et al., 2014, 2016) and also to modeling and prediction of the chemical  
72 species of volcanic gases emitted to the surface (Bugrisser and Scaillet, 2007; Gaillard  
73 et al., 2011).

74 During magma ascent, water (H<sub>2</sub>O) dissolved as hydroxyl group and molecular  
75 water in silicate melt (e.g., Stolper, 1982; Nowak and Behrens, 1995) exsolves due to  
76 decompression and a decrease in H<sub>2</sub>O solubility, resulting in the formation of bubbles.  
77 At least two species of sulfur, S<sup>2-</sup> and S<sup>6+</sup>, dissolve into silicate melt depending on  
78 oxygen fugacity, temperature, and chemical composition (e.g., Baker and Moretti, 2011).  
79 Sulfur diffuses into the bubbles during decompression, and the partition relation of  
80 sulfur between melt and bubbles depends on pressure, temperature, and oxygen fugacity

81 (e.g., Scaillet et al., 1998; Keppler, 1999, 2010). In the fluid phase (here, “fluid” refers  
82 to the aqueous fluid phase containing sulfur), sulfur appears as several chemical species  
83 (mainly H<sub>2</sub>S and SO<sub>2</sub>). Additionally, sulfide and sulfate crystals are stable as the solid  
84 phase, depending on oxygen fugacity, when sulfur fugacity in magma is high enough.  
85 For instance, pyrrhotite is a stable phase in silicic magma under a redox condition of <  
86 ~NNO+1; anhydrite is found in more oxidized magmas (e.g., Scaillet et al., 1998;  
87 Clemente et al., 2004). Therefore, if the redox condition of magma changes during the  
88 process of decompression, the breakdown and phase transition of the crystals occur, and  
89 finally the concentration of sulfur in the melt and partition relation between melt and  
90 fluid can change.

91 In decompressing magma, the degassing of volatiles also changes the oxygen  
92 fugacity of the magma itself when the fluid phase buffers the oxygen fugacity through  
93 fluid-melt redox equilibria (Matthews et al., 1994; Humphreys et al., 2015). Based on a  
94 theoretical model, Burgisser and Scaillet (2007) demonstrated that the oxygen fugacity  
95 of magma changes during magma ascent. This model agrees with experimental results,  
96 showing that the decompression of hydrous rhyolite causes the oxidation of melt  
97 coexisting with bubbles (Humphreys et al. 2015). In contrast, the pre- and post-eruptive  
98 Fe<sup>2+</sup> contents in magma inferred from petrological analyses of natural obsidian showed  
99 that H<sub>2</sub>O degassing does not influence the ferric–ferrous ratio; hence, the redox  
100 condition does not change during magma decompression (Waters and Lange, 2016). A  
101 similar approach for tephra from the Kilauea volcano (Hawaii) showed a slight  
102 reduction of magma during its ascent; the reduction was thought to be caused by sulfur  
103 degassing (Moussallam et al., 2016). Decompression-induced reduction was also  
104 observed in the 1980–1986 eruptions of Mt. St. Helens (Blundy et al., 2008). The origin

105 of these conflicting results is as yet unclear; we need to clarify experimentally the  
106 effects of water and sulfur degassing on redox evolution.

107         There are only a few experimental studies that investigated the evolution of  
108 redox conditions during magma decompression (Fiege et al., 2014; Humphreys et al.  
109 2015). Fiege et al. (2014) experimentally quantified the effects of water and sulfur  
110 degassing on the redox condition of andesite magmas at a temperature of 1030 °C; their  
111 experiments showed that the relatively reduced magma (<QFM+2) is oxidized, and  
112 oxidized magma is reduced by degassing during decompression from 300–500 MPa to  
113 ~70 MPa. In the present study, we also investigate the evolution of redox conditions  
114 during magma ascent. We focus on the ascent of silicic magma from a shallow magma  
115 reservoir to the surface. For this, decompression experiments from 100 MPa to 10–50  
116 MPa were performed for sulfur-bearing hydrous rhyolite magma at constant  
117 decompression rates of 10 and 100 MPa h<sup>-1</sup>.

118

## 119 **METHODS**

### 120 **Starting materials**

121 As starting materials for decompression experiments, two water- and sulfur-bearing  
122 rhyolitic glasses (JR1+S-g1 and JR1+S-g2 in Table 1) were synthesized in a cold seal  
123 pressure vessel from powders of glassy rhyolite (JR-1 in GSJ geochemical reference  
124 samples; Imai et al., 1995) and sulfur (sulfur crystals, Wako Pure Chemical Industries  
125 Ltd). Approximately 1 g rhyolite powder was well-mixed with 3 mg sulfur in a mortar.  
126 An aliquot of approximately 200 mg mixture was then sealed in an Au tube (~22 mm in  
127 a length, 5 mmϕ in an outer diameter, and 4.7 mmϕ in an inner diameter) with ~10 mg  
128 water. Both sides of the tube were welded shut. Two capsules were prepared and heated

129 in a cold seal pressure vessel made of Rene41 (a nickel-based alloy) with a Ni-filler rod  
130 at a temperature of 850°C under a pressure of 100 MPa for 48 h. After this heating, the  
131 pressure vessel was isobarically cooled using compressed air. The capsules were  
132 carefully opened, and the run products (JR1+S-g1 and JR1+S-g2 in Table 1) were  
133 powdered in a mortar. A small chip of the run product was mounted in resin for SEM,  
134 EPMA, and XANES analyses. Because the volatiles were saturated under the  
135 experimental condition of this study, the fluid phase was present in the capsule. The  
136 odor of H<sub>2</sub>S gas could be discerned when the capsule was opened and the samples were  
137 crushed and powdered.

138

### 139 **Decompression experiments**

140 For the decompression experiments, the powder of the synthesized sample (~20 mg)  
141 was welded shut in an Au tube (~20 mm in a length, 2 mm $\phi$  in an outer diameter and 1.7  
142 mm $\phi$  in an inner diameter). The capsule was again heated in a cold seal pressure vessel  
143 at a temperature of 800 °C under a pressure of 100 MPa for 20 h, and then it was  
144 isothermally decompressed to 10, 30, and 50 MPa at constant decompression rates of 10  
145 and 100 MPa h<sup>-1</sup>. The pressure and decompression rates were precisely controlled using  
146 a syringe pump (PMHP 13-3000 PUMP, TOP INDUSTRIE) connected to the system.  
147 Following decompression, the sample was cooled rapidly by dropping it into a  
148 water-cooled zone in the system. For comparison, two runs were quenched without  
149 decompression (annealing experiments, runs# EQ20 and EQ20-2 in Table 1). The  
150 capsule was carefully opened; half of the run product was powdered in a mortar to allow  
151 measurement of the bulk sulfur content in the glass and crystal; the rest was mounted in  
152 resin for SEM, EPMA, SIMS and XANES analyses.

153

154 **SEM, EPMA, and EA**

155 Polished run products mounted in resin were observed using scanning electron  
156 microscopes (SEMs) (JSM-7001F, JEOL Ltd; S3400-N, Hitachi Tech Co.). The  
157 chemical composition of the glass in the run products was measured using a wavelength  
158 dispersive spectroscopy electron probe microanalyzer (EPMA) (JXA-8800 M, JEOL  
159 Ltd). The measurements were carried out using a defocused beam (10  $\mu\text{m}$  in diameter),  
160 15 kV accelerating voltage, 10 nA beam current, and a peak counting time of 10 s. The  
161  $\text{H}_2\text{O}$  and S contents were measured using secondary ion mass spectrometry (SIMS) as  
162 described below.

163 The measurements of bulk sulfur content in the glass and crystal were  
164 conducted for the powdered samples using a Flash 2000 Elemental Analyzer (EA)  
165 (Thermo Fisher Scientific Inc.) (Culmo, 1972). Approximately 5–8 mg of the crushed  
166 sample powder was used for each measurement. For the synthesized glasses, JR1+S-g1  
167 and JR1+S-g2, the bulk sulfur contents could be analyzed five and three times,  
168 respectively, resulting in a relative error of 5–6%. For post-decompression run products,  
169 duplicate analysis was difficult, and the precision of the analysis is estimated to be  
170  $\pm 20\%$  at most.

171

172 **SIMS**

173 The  $\text{H}_2\text{O}$  and S contents in the glass parts of run products were analyzed at LPS Kyoto  
174 University using secondary ion mass spectrometry (SIMS; Cameca ims-4fE7). We had  
175 two different sessions for the measurements of the  $\text{H}_2\text{O}$  and S contents, because the  
176 analytical conditions used were different. We carefully checked the measurement areas

177 in run products before the SIMS analyses, because run products have a fine texture due  
178 to vesiculation and include small sulfide crystals; the data that were influenced by  
179 bubbles and crystals are not reported here.

180 SIMS analyses for hydrogen are often limited by a background signal  
181 introduced when hydrogen species in the primary ion beam strike the sample surface  
182 and are subsequently ionized during sputtering. To eliminate interference of the  
183 hydrogen species, the primary ion beam was mass-filtered to produce  $^{16}\text{O}^-$  ions,  
184 accelerated to 17.5 keV with a beam spot diameter set to 20–30  $\mu\text{m}$ , and adjusted for a  
185 beam current of approximately 10 nA. To remove the signal from the adsorbed water  
186 from the edge of the crater of the primary beam, secondary ions were generated from  
187 the center of the primary beam irradiation area (7  $\mu\text{m}$  in diameter) using a mechanical  
188 field aperture.

189 Background signals for secondary hydrogen ions are also introduced by the  
190 residual hydrogen species in the vacuum of the sample chamber. The vacuum of a  
191 sample chamber was maintained at  $3 \times 10^{-8}$  Pa with a large liquid nitrogen cold trap  
192 built by Techno-IS Corporation; this was employed to reduce background signals due to  
193 contaminated residual gases and to improve the vacuum level of species in the vicinity  
194 of the sample. A voltage offset removes background  $\text{H}^+$  counts by eliminating  $\text{H}^+$  ions  
195 desorbed from the sample surface via abundant secondary electrons produced during the  
196 impact of the primary ion beam. Kinetic energy filtering to eliminate such interference  
197 was achieved by offsetting the sample accelerating voltage (–100 eV) while keeping the  
198 setting of the electrostatic analyzer voltage and the width and position of the energy slit  
199 constant. The energy slit was set to accept a 20 eV window. Positive secondary  $^1\text{H}^+$  and  
200  $^{30}\text{Si}^+$  ions were collected sequentially with an electron multiplier to calculate the  $^1\text{H}/^{30}\text{Si}$



201 ratio. Secondary  $^1\text{H}^+$  and  $^{30}\text{Si}^+$  ions were measured for 1 s and 1 s for each cycle,  
202 respectively. The sequence was performed for 10 cycles. The mass resolution of  $M/\Delta M$   
203 was set to  $\sim 500$ .

204 For quantitative analysis, four rhyolitic glasses (SAI2, SAI3, SAI5, and SAI6  
205 in Okumura and Nakashima, 2005) were prepared as standards of known  $\text{H}_2\text{O}$  contents  
206 determined by Karl-Fischer titration. The  $\text{H}_2\text{O}$  contents of these glasses were 1.87, 1.60,  
207 0.52, and 2.56 wt%, respectively. The typical secondary ion intensities from the  
208 standard SAI2 were  $\sim 4.5$  kcps and  $\sim 7$  kcps for  $^1\text{H}$  and  $^{30}\text{Si}$ , respectively. The  $\text{H}_2\text{O}$   
209 contents of the samples were determined based on a calibration line between the  
210 secondary ion intensity ratio of  $^1\text{H}/^{30}\text{Si}$  and the  $\text{H}_2\text{O}$  content of the standards. The  
211 calibration line obtained shows good linearity (supplemental Fig. S1a); therefore, the  
212 uncertainty is thought to be relatively small, even if the calibration line is applied to  
213 higher water contents.

214 Sulfur content analyses were also performed using Cameca ims-4fE7 SIMS at  
215 LPS, Kyoto University. The primary ion beam was mass-filtered to produce  $^{133}\text{Cs}^+$  ions,  
216 accelerated to 14.5 keV with a beam spot diameter set to 20–30  $\mu\text{m}$  and adjusted for a  
217 beam current of approximately 10 nA. Secondary ions,  $^{32}\text{S}^-$  and  $^{30}\text{Si}^-$  ions, generated  
218 from the center of the primary beam irradiation area (7  $\mu\text{m}$  diameter) were eliminated  
219 using a mechanical field aperture. A normal incidence electron gun was applied to  
220 compensate electrical charge build-up of the analysis area. For quantitative analysis,  
221 four synthetic basaltic glasses, vol-0B, vol-005B, vol-1B, and vol-3A (Shimizu et al.,  
222 2017), were measured as standards (supplemental Fig. S1b). We used standard samples  
223 with basaltic composition, but the matrix effect is negligible for the S measurement in  
224 the concentration range of samples investigated in this study as shown in Shimizu et al.

225 (2017).

226

## 227 XANES

228 To determine the  $\text{Fe}^{3+}/\text{Fe}_{\text{total}}$  ratio, Fe K-edge XANES spectra were measured in the  
229 fluorescence mode at room temperature using the BL-4A beamline at the Photon  
230 Factory, High Energy Accelerator Research Organization (KEK), Japan. The current of  
231 the X-ray storage ring was 450 mA. Monochromatic excitation energy was obtained  
232 using a Si (111) double-crystal monochromator. The X-rays were focused on a 6  $\mu\text{m}$   
233 (horizontal)  $\times$  4  $\mu\text{m}$  (vertical) area via Kirkpatrick-Baez mirror optics. The samples  
234 were fixed to a sample holder positioned at an angle of  $45^\circ$  to the incident beam. The  
235 intensity of the X-ray fluorescence generated from a sample ( $I_f$ ) was measured using a  
236 Si (Li) solid-state detector. The intensity of the incident beam ( $I_0$ ) was monitored in an  
237 ion chamber filled with air. The data were collected at 1 eV intervals in the ranges of  
238 7050–7103 eV and 7119–7300 eV and 0.1 eV in the range of 7103–7119 eV. Each scan  
239 required  $\sim 40$  min.

240 The  $I_f/I_0$  ratios obtained were normalized using the average  $I_f/I_0$  ratio in the  
241 range of 7200–7300 eV. This procedure canceled the effect of the Fe concentration. In  
242 this study, we focused on a small pre-edge absorption feature observed in the 7109–  
243 7115 eV range. The pre-edge feature is derived from the 1s-3d electron transition and its  
244 shape is sensitive to the ratio of  $\text{Fe}^{3+}/\text{Fe}_{\text{total}}$  (Wilke et al., 2001; Kelley and Cottrell,  
245 2009). The pre-edge feature was deconvolved into two Gaussian curves corresponding  
246 to  $\text{Fe}^{2+}$  and  $\text{Fe}^{3+}$  components after subtraction of a linear baseline and background with  
247 a damped harmonic oscillator function (Cottrell et al. 2009). We followed the  
248 deconvolution method of Cottrell et al. (2009) to determine the relative intensity

249 between the two Gaussian curves,  $R$ , defined as the area ratio of the  $\text{Fe}^{3+}$ -derived  
250 Gaussian curve to the sum of two Gaussian curves. Here, we used the area ratio  $R$  for  
251 quantitative  $\text{Fe}^{3+}/\text{Fe}_{\text{total}}$  analysis, because it is not influenced by energy drift over time.

252 To obtain the relationship between  $R$  and the  $\text{Fe}^{3+}/\text{Fe}_{\text{total}}$  ratio, we analyzed  
253 standard samples of rhyolitic glass on loan from the National Museum of Natural  
254 History, Smithsonian Institution. The linear relationship between  $R$  and the  $\text{Fe}^{3+}/\text{Fe}_{\text{total}}$   
255 ratio, represented by  $\text{Fe}^{3+}/\text{Fe}_{\text{total}} = (1.50 \pm 0.13) \times R - (0.54 \pm 0.06)$ , was used to  
256 determine the  $\text{Fe}^{3+}/\text{Fe}_{\text{total}}$  ratio of the run product (Fig. 1). Duplicate analyses of the  
257 same sample caused an error of  $\sim 0.01$  in the  $\text{Fe}^{3+}/\text{Fe}_{\text{total}}$  ratio. In addition, the  $\text{Fe}^{3+}/\text{Fe}_{\text{total}}$   
258 ratio obtained from the same decompression run condition agreed within an error range  
259 of 0.02–0.06 (Table 1). However, the calibration line caused an error of  $\pm 0.1$  in the  
260  $\text{Fe}^{3+}/\text{Fe}_{\text{total}}$  ratio, which is almost the same as the error reported by Humphreys et al.  
261 (2015). Therefore, we conclude that the analytical error in the  $\text{Fe}^{3+}/\text{Fe}_{\text{total}}$  ratio yielded  
262 from the XANES analyses is within  $\pm 0.03$  and the relative relation of data can be  
263 discussed with an error of  $\pm 0.03$ , although the absolute value in the  $\text{Fe}^{3+}/\text{Fe}_{\text{total}}$  ratio  
264 includes an uncertainty of  $\pm 0.1$  because of the calibration line.

265 The  $f\text{O}_2$  conditions recorded in the sample were calculated based on the  
266  $\text{Fe}^{3+}/\text{Fe}_{\text{total}}$  ratio and the empirical relationship between the  $\text{Fe}^{3+}/\text{Fe}_{\text{total}}$  ratio and  $f\text{O}_2$   
267 (Kress and Carmichael, 1991) (Table 1). The calculated  $f\text{O}_2$  was compared with that of  
268 the Ni–NiO solid reaction (NNO). Because the pressure effect on NNO is small in the  
269 range of this study (Campbell et al., 2009), we used the  $f\text{O}_2$  value of NNO at 1 bar  
270 (O'Neill and Pownceby, 1993). As discussed below, the  $f\text{O}_2$  values calculated for run  
271 products without decompression, i.e., NNO+0.5 and NNO+0.87 (runs# EQ20 and  
272 EQ20-2 in Table 1), are consistent with the fact that the  $f\text{O}_2$  in our experiments was

273 buffered to ~NNO using a Ni-filler rod and that Fe sulfide crystals are stable in run  
274 products, indicating that  $fO_2$  is lower than ~NNO+2 (e.g., Parat et al., 2011). Hence, we  
275 use the  $fO_2$  values calculated based on the empirical relationship reported by Kress and  
276 Carmichael (1991), although for rhyolitic compositions, considerable uncertainty exists  
277 regarding the empirical relationship between the  $Fe^{3+}/Fe_{total}$  ratio and  $fO_2$  (Borisov et al.,  
278 2018). When “Model 4” developed by Borisov et al. (2018) is applied to our data  
279 (although the application of Model 4 to felsic magma (>68 wt%  $SiO_2$ ) is not  
280 recommended), the calculated  $fO_2$  values are 1–2 log units higher than those calculated  
281 according to the empirical relationship reported by Kress and Carmichael (1991).

282

### 283 **The timescale of $fO_2$ change by $H_2$ diffusion through Au capsules**

284 In this work, we used a Rene-type pressure vessel and a Ni-filler rod for decompression  
285 experiments; hence, redox conditions in the capsule were roughly buffered to NNO  
286 when the sample was at equilibrium in experimental conditions. Indeed, the  $fO_2$   
287 estimated from  $Fe^{3+}/Fe_{total}$  in run products without decompression is NNO to NNO+1  
288 (Table 1). For decompression experiments, we expect that the capsule was in the  
289 closed-system and that the redox condition recorded in the run product reflected the  $fO_2$   
290 change in magma during decompression, not the  $fO_2$  change outside the capsule.  
291 However, the redox condition of samples in the capsules might possibly have been  
292 changed by interaction with fluid (water, in this study) outside the capsule during  
293 decompression; this is because hydrogen can diffuse in metallic capsules. Humphreys et  
294 al. (2015) assumed that the degree of interaction is small for experimental periods of  
295 17–117 min when Pt was used at a temperature of 900 °C and neglected this effect on  
296 run products. Our experiments were conducted in an Au capsule at a temperature of 800

297 °C for 30–54 and 300–540 min for decompression rates of 100 and 10 MPa h<sup>-1</sup>,  
298 respectively; therefore, because H<sub>2</sub> diffusivity in the conditions of this study is much  
299 lower than that in Pt at 900°C, we also expect that the change in *f*O<sub>2</sub> outside the capsule  
300 would not influence the samples within the capsule. To confirm this, we experimentally  
301 investigated the timescale of *f*O<sub>2</sub> change in an Au capsule using a double capsule  
302 method (e.g., Keppler, 2010). In that experiment, the mixture of glassy rhyolite (JR1)  
303 and CuS powders was sealed in an Au tube with an outer diameter of 3 mmϕ together  
304 with a known amount of water (~3 wt%). The bulk sulfur content was controlled at  
305 ~5000 ppm. This capsule was set in an outer Au capsule with an outer diameter of 5  
306 mmϕ with hematite powder (~300 mg) and water (10 mg). The outer capsule was also  
307 welded shut and the sample was heated at a temperature of 800°C under 100 MPa for 15  
308 h. After the experiments, the run product was observed using SEM and its Fe<sup>3+</sup>/Fe<sub>total</sub>  
309 ratio was measured using XANES (Table 2). In this experiment, the sample in the inner  
310 capsule was oxidized from the rim of the sample, because the *f*O<sub>2</sub> outside the inner  
311 capsule, i.e., inside the outer capsule, was oxidized more due to the hematite buffer.

312         The experimental results are listed in Table 2 and summarized in Figure 2. The  
313 SEM image of the run product clearly indicates that Fe-Cu sulfide crystals are found in  
314 the central portion but not at a region 100–150 μm from the sample rim (Fig. 2a). The  
315 distribution of Fe<sup>3+</sup>/Fe<sub>total</sub> in the glass parts of the run product indicates that the  
316 oxidation front reached 100–150 μm inside from the sample rim (Fig. 2b). The  
317 migration of the oxidation front in magma is controlled by the H<sub>2</sub> diffusion and  
318 oxidation reaction at the front (e.g., Gaillard et al., 2003). In our experiment, the oxygen  
319 left in the capsule, and the oxygen reacted with iron and sulfur due to the H<sub>2</sub> diffusion to  
320 the outside of the sample. The rate-limiting process for the migration of the oxidation

321 front, i.e., diffusion or reaction, cannot be identified only from the experimental results  
322 obtained here. However, based on the following consideration, we infer that the  
323 migration rate is low during the decompression experiments, and the sample in the  
324 capsule was not influenced by the  $fO_2$  change of the outside of the capsule. If the  
325 migration rate is controlled by diffusion, the migration velocity ( $D_a$ ) is roughly  
326 estimated to be  $\sim 2 \mu\text{m}^2 \text{s}^{-1}$  based on the relationships of  $D_a = 5 \times D$  and  $D \sim L^2/t$ , where  
327  $D$  is the apparent diffusivity,  $L$  is the length of migration ( $\sim 150 \mu\text{m}$ ),  $t$  is the time (15 h).  
328 The factor of five is included to explain the difference in bulk sulfur content. When we  
329 apply this velocity to the decompression experiments, only the 80 and 255  $\mu\text{m}$  distances  
330 from the capsule are influenced by the change of  $fO_2$  for the decompression experiments  
331 at 100 and 10 MPa  $\text{h}^{-1}$ , respectively. Even if the migration rate is limited by the reaction,  
332 the region influenced by the change of  $fO_2$  during decompression is small if the  
333 rate-limiting reaction during decompression is the same as with the oxidation  
334 experiment. Based on this estimate, we concluded that the sample in the capsule was not  
335 influenced by the change in the  $fO_2$  outside of the capsule during decompression, except  
336 for sample margin; hence, the sample mainly records the change in  $fO_2$  of magma  
337 during decompression and the XANES analyses were carried out for the central portion  
338 of the samples.

339

## 340 **RESULTS**

### 341 **The texture of run products**

342 Figures 3 and 4 indicate reflected light and backscattered electron images of run  
343 products. The synthesized starting material (JR1+S-g1) and run product annealed at 800  
344  $^{\circ}\text{C}$  and 100 MPa for 20 h (run# EQ20) include bubbles (Figs. 3a,b and 4a,b). This

345 indicates that bubbles existed in the melt before decompression. The images of run  
346 products after decompression show that the bubble size increased with decompression,  
347 resulting in coalescence (Figs. 3c,d and 4c,d). The bubbles in run products  
348 decompressed at  $100 \text{ MPa h}^{-1}$  (Fig. 3c) are slightly smaller than those decompressed at  
349  $10 \text{ MP h}^{-1}$  (Fig. 3d) when compared at the same final pressure.

350 Tubular Fe sulfide crystals are also found in the run products as well as the  
351 starting material (Fig. 4). The Fe sulfides were identified using an energy-dispersive  
352 X-ray spectroscopy; however, the exact composition was difficult to determine, because  
353 the surrounding glass influenced the results due to the small size of the crystals. The Fe  
354 sulfide crystals are found in all run products.

355

### 356 **Chemical composition and H<sub>2</sub>O and S contents**

357 Major element composition and H<sub>2</sub>O and S contents in glass parts of run products are  
358 listed in Table 1. The major element compositions of the glass parts are almost the same  
359 as the recommended value of JR1, except for the decrease in FeO content. The decrease  
360 in FeO content is caused by the formation of the Fe sulfide, as found in run products  
361 (Fig. 4). When we compare the differences between the FeO content in the synthesized  
362 glass for decompression experiments (starting material) with the recommended value of  
363 JR1 (FeO = 0.8 wt%), the differences are 0.24 and 0.19 wt% under the anhydrous  
364 normalized value for JR1+S-g1 and JR1+S-g2, respectively (Table 1 and supplemental  
365 Table S1). Assuming that all Fe was consumed in the formation of the Fe sulfide  
366 crystals (we assumed pyrrhotite based on phase relation at our experimental condition;  
367 Parat et al., 2011) and the densities of hydrous rhyolite glass and pyrrhotite are  $2300 \text{ kg}$   
368  $\text{m}^{-3}$  (Okumura and Nakashima, 2005) and  $4600 \text{ kg m}^{-3}$ , respectively, the volume

369 fraction of the Fe sulfide crystals is estimated to be 0.1–0.2 vol% based on mass balance  
370 calculation. Based on the mass balance, total S contents in the Fe sulfide crystals are  
371 also estimated to be 0.107 and 0.085 wt% for JR1+S-g1 and JR1+S-g2, respectively  
372 (Table 1). Because the S content in the glass part is low, these values should be almost  
373 equal to bulk sulfur content in quenched run products. Indeed, the measured bulk sulfur  
374 concentrations (1056 and 1061 ppm for JR1+S-g1 and JR1+S-g2, respectively, in Table  
375 1) are almost consistent with the estimated values above. This result also means that the  
376 two-thirds of sulfur mass in a capsule was distributed in the fluid phase because the S  
377 content was roughly controlled at 3000 ppm by mixing 1 g of JR1 powder and 3 mg of  
378 elemental sulfur. No clear change in other elements, i.e., calcium, indicates that the  
379 sulfate crystal is not formed or its abundance is low.

380 In decompression experiments, the starting materials were annealed at 800°C  
381 and 100 MPa for 20 h again, then decompressed to final pressure. Two runs without  
382 decompression were also performed to determine the effect of annealing. The bulk S  
383 content decreased after annealing, corresponding to a small increase of Fe content in the  
384 glass (run# EQ20 and EQ20-2 in Table 1). Because S content in the glass was lower  
385 than those degassed during the annealing, the sulfur was distributed into the fluid phase  
386 again (Table 1). In fact, the annealed samples show bubbles in run products (Figs. 3b  
387 and 4b). This means that the sulfur-bearing fluid phases coexisted just before  
388 decompression in this study.

389 For run products after decompression, the relationship between H<sub>2</sub>O content in  
390 glass and pressure is shown in Fig. 5a, together with the H<sub>2</sub>O solubility curve of  
391 hydrous rhyolitic melt at a temperature of 800 °C (Newman and Lowenstern, 2002).  
392 The H<sub>2</sub>O content decreased with decompression, and the decreasing trend of the H<sub>2</sub>O



393 content is comparable to those predicted from the model of Newman and Lowenstern  
394 (2002); this indicates that dehydration during the decompression was almost at  
395 equilibrium. Small errors in the H<sub>2</sub>O content measured at some points in a run product  
396 (Table 1) indicate homogeneous H<sub>2</sub>O distribution, suggesting that H<sub>2</sub>O diffusion was  
397 fast and the dehydration was almost at equilibrium.

398         The H<sub>2</sub>O contents measured are slightly higher than that predicted by the H<sub>2</sub>O  
399 solubility model of Newman and Lowenstern (2002), in which the S effect was not  
400 considered. When we estimate H<sub>2</sub>O solubility based on different H<sub>2</sub>O solubility model  
401 (Liu et al., 2005), the difference in the H<sub>2</sub>O contents estimated by models of Newman  
402 and Lowenstern (2002) and Liu et al. (2005) is only ~0.02 wt% in the studied pressure  
403 range. The mechanism of the increase in H<sub>2</sub>O solubility by the addition of S to the  
404 system is unclear as of yet, but the increase in H<sub>2</sub>O solubility in sulfur-bearing  
405 rhyodacite has also been reported by Botcharnikov et al. (2004). In contrast, Webster et  
406 al. (2011) demonstrated that H<sub>2</sub>O solubility decreases by adding S in haplogranitic melts  
407 under reduced conditions (<NNO+0.3). Thus, additional experiments are required to  
408 quantify the effect of S on H<sub>2</sub>O solubility in felsic melts.

409         The S content in glass slightly decreased with decompression from 100 to 50  
410 MPa; it shows an almost constant value (13–19 ppm) at pressures <50 MPa (Fig. 5b).  
411 The S solubility estimated based on the model of Burgisser et al. (2015) shows a  
412 decrease with pressure. The deviation from the model at 10 MPa may be caused by  
413 disequilibrium degassing due to the slow diffusion of sulfur in silicate melt compared  
414 with the diffusion of water (Baker et al., 2005; Zhang et al., 2007); however, the  
415 solubility law of sulfur at low pressure is not well established due to a lack of  
416 experimental data; hence, the origin of the difference between our data and model

417 predictions should be investigated in future studies.

418 Bulk S contents show 454–997 ppm for all the samples, and no clear change is  
419 found during decompression (Fig. 5c). The S content in glass measured by SIMS is  
420 much lower than bulk S content; hence, these results indicate that the main S source in  
421 bulk S content was the Fe sulfide crystals and the sulfide crystals were stable during  
422 decompression.

423

#### 424 **Fe<sup>3+</sup>/Fe<sub>total</sub> ratios and redox conditions**

425 The Fe<sup>3+</sup>/Fe<sub>total</sub> ratios obtained are listed in Table 1. Figure 6a shows the evolution of the  
426 Fe<sup>3+</sup>/Fe<sub>total</sub> ratios in glasses through decompression. Before decompression, the  
427 Fe<sup>3+</sup>/Fe<sub>total</sub> ratio was 0.33–0.36. The ratio slightly decreased with decompression,  
428 indicating a slight reduction with decompression. At the pressure of 10 MPa, the  
429 Fe<sup>3+</sup>/Fe<sub>total</sub> ratio is 0.22–0.24, which is clearly smaller than those of initial condition  
430 (0.33–0.36). The decompression rate does not influence the result.

431 Based on the measured Fe<sup>3+</sup>/Fe<sub>total</sub> ratios, the *f*O<sub>2</sub> conditions recorded in the  
432 samples were calculated using the empirical relationship between the Fe<sup>3+</sup>/Fe<sub>total</sub> ratio  
433 and *f*O<sub>2</sub>. The experimental data indicate that the *f*O<sub>2</sub> was buffered at NNO+0.5 to  
434 NNO+0.9 before decompression; it slightly decreased with decompression, resulting in  
435 NNO–0.6 to NNO–0.8 at 10 MPa (Fig. 6b).

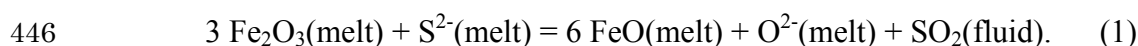
436

#### 437 **DISCUSSIONS**

438 Our experiments clearly demonstrated that rhyolitic magma shows a slight reduction  
439 with decompression (Fig 6b). However, Humphreys et al. (2015) experimentally  
440 showed that hydrous rhyolitic magma could be oxidized during decompression. This

441 difference is caused by sulfur in our experimental system, which was not included in the  
442 experiments of Humphreys et al. (2015). A possible explanation for magma reduction is  
443 the direct effect of sulfur degassing represented by the following reaction (e.g., Blundy  
444 et al., 2008; Metrich et al., 2009):

445



447

448 The contribution of this reaction to melt reduction is calculated based on the mass  
449 balance. In our experiment, the decrease in the S content in melt is ~17 ppm during  
450 decompression from 100 to 10 MPa (Fig. 5b); stoichiometric calculation according to  
451 reaction 1 results in a decrease in Fe<sub>2</sub>O<sub>3</sub> of ~255 ppm. Therefore, only a few percentage  
452 of total iron could have been reduced by this reaction, because total iron content is ~0.6  
453 wt% (Table 1). This reduction is smaller than the observed change, that is, Fe<sup>3+</sup>/Fe<sub>total</sub> =  
454 0.33 and 0.36 before decompression and Fe<sup>3+</sup>/Fe<sub>total</sub> = 0.22 and 0.24 at 10 MPa with a  
455 decompression rate of 100 MPa h<sup>-1</sup> (Table 1); hence, magma reduction during  
456 decompression cannot be explained only by reaction 1.

457 In addition to reaction 1, fluid-melt equilibria during decompression can  
458 change *f*O<sub>2</sub> in the system (e.g., Matthews et al., 1994; Burgisser and scaillet, 2007;  
459 Moussallam et al., 2014, 2016). To compare our data with *f*O<sub>2</sub> estimated based on  
460 fluid-melt equilibria, we calculated the evolution of the redox condition of  
461 sulfur-bearing hydrous rhyolitic magma using the thermodynamic model of Burgisser et  
462 al. (2015) (Fig 6b). This model considers the reaction of the H-O-S system in fluid  
463 phase and empirical solubility laws for H<sub>2</sub>O, H<sub>2</sub>S, and SO<sub>2</sub>; *f*O<sub>2</sub> is calculated in  
464 equilibrium condition. It should be noted that empirical parameters for the H<sub>2</sub>S and SO<sub>2</sub>

465 solubility laws were obtained based on experimental data obtained at ~200 MPa  
466 reported by Clemente et al. (2004); therefore, the estimates at low pressure may include  
467 large uncertainties.

468           In this calculation, an important parameter is the pre-exsolved fluid phase (Fig.  
469 6b). When a pre-exsolved fluid phase coexists before decompression, sulfur is strongly  
470 distributed into the fluid phase under the reducing condition (Keppler, 2010); the fluid  
471 phase, including sulfur, influences the evolution of the redox condition. At the initial  $fO_2$   
472 of NNO+1 to NNO, the model prediction indicates no change of  $fO_2$  or a slight  
473 reduction when the sample includes the fluid phase of ~10 vol% before decompression,  
474 which is equivalent to that in run products without decompression. In contrast, when  
475 almost no fluid phase exists before decompression (0.1 vol% in Fig. 6b), magma is  
476 slightly reduced and then oxidized during decompression at initial  $fO_2$  of NNO+1 and  
477 continuously oxidized through decompression at the initial  $fO_2$  of NNO. If we assume  
478 only water in the system, then the model also shows that the magma is strongly oxidized  
479 (Fig. 6b). These results clearly indicate that the sulfur in the system controls the  
480 evolution of redox conditions during magma decompression. The pre-exsolved fluid  
481 phase in which sulfur partition occurs strongly, in particular, reduces the magma, while  
482 magma without the pre-exsolved fluid phase is oxidized even if it contains a small  
483 amount of sulfur. The reduction of magma during decompression can be attributed to  
484 the direct effect of sulfur degassing (reaction 1) and fluid-melt equilibria (Fig. 6b).  
485 However, the degree of reduction found experimentally could not be reproduced by  
486 these models; hence, additional experimental works at low pressure and comparison  
487 with the modeled results are necessary.

488           Decompression experiments by Fiege et al. (2014) showed that andesitic

489 magma is oxidized with decompression from 300–500 to ~70 MPa when the magma is  
490 under reducing conditions just before the decompression (<QFM+2, corresponding to  
491 ~<NNO+1). Fiege et al. (2014) demonstrated redox changes based on experimentally  
492 determined  $fO_2$  and  $S^{6+}/S_{total}$  values measured by XANES. However, if we focus on only  
493 the  $Fe^{3+}/Fe_{total}$  values in Fiege et al. (2014), most of the  $Fe^{3+}/Fe_{total}$  values show  
494 decreases during decompression under both reducing and oxidation conditions (Table 2  
495 and Fig. 4b in Fiege et al., 2014). Therefore, our observation that decompression causes  
496 a decrease in  $Fe^{3+}/Fe_{total}$  seems consistent with their data. To clarify the origin of the  
497 different behaviors of  $S^{6+}/S_{total}$  and  $Fe^{3+}/Fe_{total}$ , additional analyses and experiments are  
498 needed; however, these results clearly indicate that the sulfur in the system causes  
499 complicated processes, and the inclusion of the effect of sulfur is necessary for  
500 understanding the evolution of redox conditions during magma ascent.

501

## 502 **IMPLICATIONS**

503 Our experiments indicated that sulfur-bearing hydrous rhyolite magma with a  
504 pre-exsolved fluid phase experiences a slight reduction during magma ascent. In our  
505 experiments, the S content in melt before decompression was ~30 ppm, which is within  
506 the range of natural silicic magmas (Wallace, 2005). The total S content in studied  
507 magmas including sulfur in fluid phase, i.e., ~1000 ppm, also reproduced a part of  
508 natural system (e.g., Keppler, 1999; Kilbride et al., 2016). The decompression rates  
509 simulated in this study (10 and 100 MPa h<sup>-1</sup>) corresponded to those during explosive  
510 eruptions and effusive eruptions (Rutherford and Hill, 1993; Liu et al., 2007; Noguchi et  
511 al., 2008; Rutherford, 2008). Therefore, the ascent of H<sub>2</sub>O- and S-bearing magmas with  
512 rhyolitic melts in nature was simulated by our experiments.

513           During explosive eruptions, magma experiences closed-system degassing  
514 because of its high ascent rate, as simulated in the experiment; therefore, we infer that  
515 magma experiences a slight reduction during the ascent in explosive eruptions. In  
516 contrast, the redox evolution during effusive eruptions seems to be more complicated,  
517 because magma can experience both closed- and open-system degassing, i.e., repeated  
518 degassing and compaction processes, during its ascent (Eichelberger et al., 1986;  
519 Okumura et al., 2009, 2010). Because sulfur strongly partitions in the fluid phase,  
520 open-system degassing in the early stages may release a sulfur-bearing fluid phase, then  
521 the fluid phase contains a small amount of the sulfur at the later stages. In this case,  
522 magma can be oxidized by the degassing process at the later stages.

523           Our experiments also indicated that decompression does not result in the  
524 breakdown of sulfide crystals; hence, we infer that sulfide minerals, stable in silicic  
525 magma reservoirs in the shallow crust, survive during magma ascent. However, the  
526 breakdown texture has been found in pyroclasts and lavas, and this is sometimes  
527 thought to be caused by decompression (e.g., Larocque et al., 2000; Di Muro et al.,  
528 2008). This may be explained by the oxidation caused by repeated degassing and  
529 compaction processes, as well as the decrease of sulfur fugacity during open-system  
530 degassing. Based on our experiments and these considerations, we conclude that to  
531 determine the redox condition of magma reservoirs, the redox condition must be tracked  
532 back quantitatively by considering fluid composition, pre-exsolved fluid phases, and  
533 degassing processes.

534

535 *Acknowledgments.* We would like to thank Maxim Gavrilenko and Kayla Iacovino for  
536 their constructive reviews. We would like to thank Elizabeth Cottrell and the National

537 Museum of Natural History's Rock Collection for the loan of the standards for XANES.  
538 We are grateful to Atsuo Iida for his technical suggestions. This study was supported by  
539 the Grants-in-aid for Scientific Research in Japan (No. 15K13587 and 18H01296) to  
540 SO.

541

#### 542 References

543 Baker, D.R., Freda, C., Brooker, R., and Scarlato, P. (2005) Volatile diffusion in silicate  
544 melts and its effects on melt inclusions, *Annals of Geophysics*, 48, 699–717.

545 Baker, D., and Moretti, R. (2011) Modeling the solubility of sulfur in magmas: A  
546 50-year old geochemical challenge. *Reviews in Mineralogy and Geochemistry*,  
547 73, 167–213.

548 Blundy, J., Cashman, K.V., and Berlo, K. (2008) Evolving Magma Storage Conditions  
549 Beneath Mount St. Helens Inferred from Chemical Variations in Melt  
550 Inclusions from the 1980–1986 and Current (2004–2006) Eruptions, U.S.  
551 Geological Survey Professional Paper 1750, 755–790.

552 Borisov, A., Behrens, H., and Holtz, F. (2018) Ferric/ferrous ratio in silicate melts: a  
553 new model for 1 atm data with special emphasis on the effects of melt  
554 composition, *Contribution to Mineralogy and Petrology*, 173, 98.

555 Botcharnikov, R. E., Behrens, H., Holtz, F., Koepke, J., and Sato, H. (2004) Sulfur and  
556 chlorine solubility in Mt. Unzen rhyodacitic melt at 850°C and 200 MPa,  
557 *Chemical Geology*, 213, 207–225.

558 Burgisser, A., and Scaillet, B. (2007). Redox evolution of a degassing magma rising to  
559 the surface. *Nature*, 445, 194–197.

560 Burgisser, A., Alletti, M., and Scaillet, B. (2015) Simulating the behavior of volatiles

- 561 belonging to the C–O–H–S system in silicate melts under magmatic conditions  
562 with the software D-Compress, Computers & Geosciences, 79, 1–14.
- 563 Campbell, A.J., Danielson, L., Richter, K., Seagle, C.T., Wang, Y., and Prakapenka, V.B.  
564 (2009) High pressure effects on the iron–iron oxide and nickel–nickel oxide  
565 oxygen fugacity buffers, Earth Planetary Science Letters, 286, 556–564.
- 566 Carmichael, I.S.E. (1991) The redox states of basic and silicic magmas: a reflection of  
567 their source regions? Contribution to Mineralogy and Petrology, 106, 129–141.
- 568 Carmichael, I.S.E., and Ghiorso, M.S. (1990) The effect of oxygen fugacity on the  
569 redox state of natural liquids and their crystallizing phases, Reviews in  
570 Mineralogy and Geochemistry, 24, 191–212.
- 571 Clemente, B., Scaillet, B., and Pichavant, M. (2004) The solubility of sulfur in hydrous  
572 rhyolitic melts, Journal of Petrology, 45, 2171–2196.
- 573 Clumo, R.F. (1972) The microdetermination of sulfur with an automatic element  
574 analyzer, Microchemical Journal, 17, 499–507.
- 575 Cottrell, E., Kelley, K.A., Lanzirotti, A., Fischer, R.A. (2009) High-precision  
576 determination of iron oxidation state in silicate glasses using XANES.  
577 Chemical Geology, 268, 167–179.
- 578 Di Muro, A., Pallister, J., Villemant, B., Newhall, C., Semet, M., Martinez, M., and  
579 Mariet, C. (2008) Pre-1991 sulfur transfer between mafic injections and dacite  
580 magma in the Mt. Pinatubo reservoir, Journal of Volcanology and Geothermal  
581 Research, 175, 517–540.
- 582 Eichelberger, J.C., Carrigan, C.R., Westrich, H.R., and Price, R.H. (1986)  
583 Non-explosive silicic volcanism. Nature, 323, 598–602.
- 584 Fiege, A., Behrens, H., Holtz, F., and Adams, F. (2014) Kinetics vs. thermodynamic



- 585 control of degassing of H<sub>2</sub>O–S±Cl-bearing andesitic melts, *Geochimica et*  
586 *Cosmochimica Acta*, 125, 241–264.
- 587 Gaillard, F., Schmidt, B., Mackwell, S., and McCammon, C. (2003) Rate of  
588 hydrogen-iron redox exchange in silicate melts and glasses, *Geochimica et*  
589 *Cosmochimica Acta*, 67, 2427–2441.
- 590 Gaillard, F., Scaillet, B., and Arndt, N.T. (2011) Atmospheric oxygenation caused by a  
591 change in volcanic degassing pressure, *Nature*, 478, 229–232.
- 592 Humphreys, M.C.S., Brooker, R.A., Fraser, D.G., Burgisser, A., Mangan, M.T., and  
593 McCammon, C. (2015) Coupled interactions between volatile activity and Fe  
594 oxidation state during arc crustal processes, *Journal of Petrology*, 56, 795–814.
- 595 Imai, N., Terashima, S., Itoh, S., and Ando, A. (1995) 1994 compilation values for GSJ  
596 reference samples, “Igneous rock series”, *Geochemical Journal*, 29, 91–95.
- 597 Kelley, K.A., and Cottrell, E. (2009) Water and the oxidation state of subduction zone  
598 magmas, *Science*, 325, 605–607.
- 599 Keppler, H. (1999) Experimental evidence for the source of excess sulfur in explosive  
600 volcanic eruptions, *Science*, 284, 1652–1654.
- 601 Keppler, H. (2010) The distribution of sulfur between haplogranitic melts and aqueous  
602 fluids, *Geochimica et Cosmochimica Acta*, 74, 645–660.
- 603 Kilbride, B.M., Biggs, J., and Edmonds, M. (2016) Observing eruptions of gas-rich  
604 compressible magmas from space, *Nature communications*, 7, 1–8.
- 605 Kress, V.C., and Carmichael, I.S.E. (1991) The compressibility of silicate liquids  
606 containing Fe<sub>2</sub>O<sub>3</sub> and the effect of composition, temperature, oxygen fugacity  
607 and pressure on their redox states, *Contribution to Mineralogy and Petrology*,  
608 108, 82–92.

- 609 Larocque, A.C.L., Stimac, J.A., Keith, J.D., and Huminicki, M.A.E. (2000) Evidence of  
610 open-system behavior in immiscible Fe–S–O liquids in silicate magmas:  
611 implications for contributions of metals and sulfur to ore-forming fluids, *The*  
612 *Canadian Mineralogist*, 38, 1233–1249.
- 613 Liu, Y., Zhang, Y., and Behrens, H. (2005) Solubility of H<sub>2</sub>O in rhyolitic melts at low  
614 pressures and a new empirical model for mixed H<sub>2</sub>O–CO<sub>2</sub> solubility in rhyolitic  
615 melts, 143, 219–235.
- 616 Liu, Y., Anderson, A.T., and Wilson, C.J. (2007) Melt pockets in phenocrysts and  
617 decompression rates of silicic magmas before fragmentation. *Journal of*  
618 *Geophysical Research*, 112, B06204, doi:10.1029/2006JB004500.
- 619 Matthews, S.J., Jones, A.P., and Beard, A.D. (1994) Buffering of melt oxygen fugacity  
620 by sulfur redox reactions in calc-alkaline magmas, *Journal of the Geological*  
621 *Society, London*, 151, 815–823.
- 622 Métrich, N., Berry, A.J., O’Neill, H.St.C., and Susini, J. (2009) The oxidation state of  
623 sulfur in synthetic and natural glasses determined by X-ray absorption  
624 spectroscopy, *Geochimica et Cosmochimica Acta*, 73, 2382–2399.
- 625 Moussallam, Y., Oppenheimer, C., Scaillet, B., Gaillard, F., Kyle, P., Peters, N., Hartley,  
626 M., Berlo, K., and Donovan, K. (2014) Tracking the changing oxidation state  
627 of Erebus magmas, from mantle to surface, driven by magma ascent and  
628 degassing, *Earth and Planetary Science Letters*, 393, 200–209.
- 629 Moussallam, Y., Edmonds, M., Scaillet, B., Peters, N., Gennaro, E., Sides, I., and  
630 Oppenheimer, C. (2016) The impact of degassing on the oxidation state of  
631 basaltic magmas: A case study of Kīlauea volcano, *Earth and Planetary Science*  
632 *Letters*, 450, 317–325.

- 633 Nowak, M., and Behrens, H. (1995) The speciation of water in haplogranitic glasses and  
634 melts determined by in situ near-infrared spectroscopy, *Geochimica et*  
635 *Cosmochimica Acta*, 59, 3445–3450.
- 636 Newman, S., and Lowenstern, J.B. (2002) VolatileCalc: a silicate melt–H<sub>2</sub>O–CO<sub>2</sub>  
637 solution model written in Visual Basic for excel, *Computers & Geosciences*, 28,  
638 597–604.
- 639 Noguchi, S., Toramaru, A., and Nakada, S. (2008) Relation between microlite textures  
640 and discharge rate during the 1991–1995 eruptions at Unzen, Japan. *Journal of*  
641 *Volcanology and Geothermal Research*, 175, 141–155.
- 642 Okumura, S., and Nakashima, S. (2005) Molar absorptivities of OH and H<sub>2</sub>O in  
643 rhyolitic glass at room temperature and at 400–600°C. *American Mineralogist*,  
644 90, 441–447.
- 645 Okumura, S., Nakamura, M., Takeuchi, S., Tsuchiyama, A., Nakano, T., and Uesugi, K.  
646 (2009) Magma deformation may induce non-explosive volcanism via  
647 degassing through bubble networks, *Earth and Planetary Science Letters*, 281,  
648 267–274.
- 649 Okumura, S., Nakamura, M., Nakano, T., Uesugi, K., and Tsuchiyama, A. (2010) Shear  
650 deformation experiments on vesicular rhyolite: Implications for brittle  
651 fracturing, degassing, and compaction of magmas in volcanic conduits, *Journal*  
652 *of Geophysical Research*, 115, B06201.
- 653 O'Neill, H.St.C., and Pownceby, M.I. (1993) Thermodynamic data from redox reactions  
654 at high temperatures. I. An experimental and theoretical assessment of the  
655 electrochemical method using stabilized zirconia electrolytes, with revised  
656 values for the Fe–"FeO", Co–CoO, Ni–NiO and Cu–Cu<sub>2</sub>O oxygen buffers, and

- 657 new data for the W–WO<sub>2</sub> buffer, *Contribution to Mineralogy and Petrology*,  
658 114, 296–314.
- 659 Parat, F., Holtz, F., and Streck, M.J. (2011) Sulfur-bearing magmatic accessory minerals,  
660 *Reviews in Mineralogy and Geochemistry*, 73, 285–314.
- 661 Rutherford, M.J. (2008) Magma ascent rates, *Reviews in Mineralogy and Geochemistry*,  
662 69, 241–271.
- 663 Rutherford, M.J., and Hill, P.M. (1993) Magma ascent rates from amphibole  
664 breakdown: An experimental study applied to the 1980–1986 Mount St. Helens  
665 eruptions, *Journal of Geophysical Research*, 98, 19667–19685.
- 666 Scaillet, B., Clemente, B., Evans, B.W., and Pichavant, M. (1998) Redox control of  
667 sulfur degassing in silicic magmas. *Journal of Geophysical Research*, 103,  
668 23937–23949.
- 669 Shimizu, K., Ushikubo, T., Hamada, M., Itoh, S., Higashi, Y., Takahashi, E., and Ito, M.  
670 (2017) H<sub>2</sub>O, CO<sub>2</sub>, F, S, Cl, and P<sub>2</sub>O<sub>5</sub> analyses of silicate glasses using SIMS:  
671 Report of volatile standard glasses. *Geochemical Journal*, 51, 299–313.
- 672 Stolper, E.M. (1982) Water in silicate melts: an infrared spectroscopic study,  
673 *Contribution to Mineralogy and Petrology*, 81, 1–17.
- 674 Wallace, P.J. (2005) Volatiles in subduction zone magmas: concentrations and fluxes  
675 based on melt inclusion and volcanic gas data. *Journal of Volcanology and*  
676 *Geothermal Research*, 140, 217–240.
- 677 Wallace, P.J., Plank, T., Edmonds, M., and Hauri, E.H. (2015) Volatiles in magma. In H.  
678 Sigurdsson, et al., Ed., *Encyclopedia of Volcano* (2nd edition), p. 163–183.  
679 Academic Press, Amsterdam.
- 680 Waters, L.E., and Lange, R.A. (2016) No effect of H<sub>2</sub>O degassing on the oxidation state

- 681 of magmatic liquids, *Earth and Planetary Science Letters*, 447, 48–59.
- 682 Webster, J.D., Goldoff, B., and Shimizu, N. (2011) C–O–H–S fluids and granitic  
683 magma: how S partitions and modifies CO<sub>2</sub> concentrations of fluid-saturated  
684 felsic melt at 200 MPa, *Contribution to Mineralogy and Petrology*, 162, 849–  
685 865.
- 686 Wilke, M., Farges, F., Petit, P.-E., Brown, G.E., and Martin, F. (2001) Oxidation state  
687 and coordination of Fe in minerals: An Fe K-XANES spectroscopic study,  
688 *American Mineralogist*, 86, 714–730.
- 689 Zhang, Y., Xu, Z., Zhu, M., and Wang, H. (2007) Silicate melt properties and volcanic  
690 eruptions, *Reviews of Geophysics*, 45, RG4004.

691

## 692 Figure captions

693 Figure 1. Relationship between R and Fe<sup>3+</sup>/Fe<sub>total</sub> obtained from samples of Cottrell et al.  
694 (2009). The dashed line represents the linear fitting of the experimental data, which  
695 gives the relation of  $R = (0.67 \pm 0.06) \times (\text{Fe}^{3+}/\text{Fe}_{\text{total}}) + (0.36 \pm 0.04)$ . This line was  
696 used as a calibration line for the XANES measurements. The samples used are  
697 568\_2, DT\_46, DT\_39, H2O\_63, DT\_31, and DT\_18 of Cottrell et al. (2009).

698 Figure 2. (a) A backscattered electron image of run product after oxidation experiment.  
699 The upper left and lower parts (black areas) correspond to the resin. Sample rims do  
700 not include sulfide crystal, while the inside of the sample contains the sulfide  
701 crystals (white particles). We measured Fe<sup>3+</sup>/Fe<sub>total</sub> at four points (diamonds) along  
702 a white line (solid diamonds in Fig. 2b). The black bar indicates a 100 μm scale. (b)  
703 Relationship between Fe<sup>3+</sup>/Fe<sub>total</sub> and distance from sample rim. Two line profiles  
704 obtained in a sample show the increase of Fe<sup>3+</sup>/Fe<sub>total</sub> toward the sample rim, which

705 clearly indicates the oxidation at sample rim. The solid diamonds represent data  
706 obtained from four points along a white line in (a). The crosses are data from five  
707 points outside image (a).

708 Figure 3. Reflected light images of (a) a starting material (JR1+S-g1), (b) a run product  
709 without decompression (annealing, run# EQ20), (c) run products decompressed to  
710 50, 30, and 10 MPa at a rate of  $100\text{MPa h}^{-1}$  (runs# 100-50, 100-30, and 100-10),  
711 and (d) run products decompressed to 50 and 30 MPa at  $10\text{ MPa h}^{-1}$  (runs# 10-50  
712 and 10-30). The white bar in (a) indicates a  $100\text{ }\mu\text{m}$  scale; the scale is the same in  
713 all the panels.

714 Figure 4. Backscattered electron images of (a) a starting material (JR1+S-g1), (b) a run  
715 product without decompression (annealing, run# EQ20), (c) run products  
716 decompressed to 50, 30, and 10 MPa at a rate of  $100\text{MPa h}^{-1}$  (runs# 100-50, 100-30,  
717 and 100-10), and (d) run products decompressed to 50 and 30 MPa at  $10\text{ MPa h}^{-1}$   
718 (runs# 10-50 and 10-30). The white bar in (a) indicates a  $10\text{ }\mu\text{m}$  scale; the scale is  
719 the same in all the panels. The white particles with tubular shape (Fe sulfide  
720 crystals) are found in all the run products as well as the starting material.

721 Figure 5. (a)  $\text{H}_2\text{O}$  and (b) S contents in glass parts of run products and (c) bulk S content  
722 in glass and crystal as a function of final run pressure. “EQ” represents data  
723 obtained from annealing experiments without decompression. The solid curve in (a)  
724 represents the  $\text{H}_2\text{O}$  solubility calculated from the model of Newman and  
725 Lowenstern (2002) (N&L solubility model). The solid and dashed curves in (b)  
726 indicate the S solubility calculated based on the model of Burgisser et al. (2015)  
727 with the assumption of initial conditions at NNO and NNO+1 and with an exsolved  
728 fluid phase of 10 vol%. The symbols in (b) and (c) are the same as those in (a). The

729 error bars represent the errors in Table 1.

730 Figure 6. (a) Evolution of  $\text{Fe}^{3+}/\text{Fe}_{\text{total}}$  in melt during decompression. The  $\text{Fe}^{3+}/\text{Fe}_{\text{total}}$   
731 slightly decreases with pressure. The analytical error ( $\pm 0.03$ ) is within the size of  
732 the symbol. (b) The change of  $f\text{O}_2$  during decompression. The  $f\text{O}_2$  value is  
733 represented on the basis of Ni-NiO buffer ( $\Delta\text{NNO}$ ). The experimental results show  
734 a slight reduction with decompression. For decompression of sulfur-bearing  
735 hydrous rhyolite magma initially buffered with NNO+1 and NNO, the theoretical  
736 predictions of  $f\text{O}_2$  change based on the thermodynamic model of Burgisser et al.  
737 (2015) are shown by solid and dashed curves, respectively. The reduction with  
738 decompression can take place when magma buffered with NNO+1 includes an  
739 exsolved fluid phase of  $\sim 10$  vol%. If magma does not have an exsolved fluid phase  
740 or the amount of exsolved fluid phase is small, magma is slightly oxidized (0.1  
741 vol%). In sulfur-free system, strong oxidation takes place even if magma has a  
742 pre-exsolved fluid (H system 10 vol% initial).

743

**TABLE 1.** Experimental condition and the summary of analytical results

	Starting material		Annealing		Decompression								JR1 std
	JR1+S-g1	JR1+S-g2	EQ20	EQ20-2	10-30	10-50	100-10	100-10-2	100-30	100-30-2	100-50	100-50-2	
Final P (MPa)	100	100	100	100	30	50	10	10	30	30	50	50	-
Rate (MPa h <sup>-1</sup> )	-	-	-	-	10	10	100	100	100	100	100	100	-
H <sub>2</sub> O <sub>glass</sub> (wt%)	-	-	4.8 (0.7) <sup>a</sup>	-	2.3 (0.4)	3.4 (0.4)	1.4 (0.2)	1.6 (0.3)	2.9 (0.5)	2.6 (0.5)	3.5 (0.4)	3.3 (0.5)	-
S <sub>glass</sub> (ppm) <sup>b</sup>	-	-	34 (10)	29 (3)	-	19 (7)	-	15 (2)	-	13 (1)	-	16 (1)	-
Bulk S (ppm) <sup>b</sup>	1089 (64)	1024 (53)	503 (101)	997 (169)	454 (91)	870 (174)	-	468 (94)	487 (97)	526 (105)	-	480 (96)	-
Fe <sup>3+</sup> /Fe <sub>total</sub>	0.30	0.39	0.33	0.36	0.27	0.31	0.22	0.24	0.24	0.30	0.31	0.33	-
ΔNNO	0.24	1.16	0.50	0.87	-0.21	0.27	-0.79	-0.56	-0.55	0.11	0.24	0.51	-
SM sample <sup>c</sup>	-	-	g1	g2	g2	g1	g1	g2	g1	g2	g1	g2	-
<b>Average</b>													
SiO <sub>2</sub> (wt%)	69.47	69.93	71.42	70.59	73.30	72.21	73.89	73.93	72.78	74.25	72.44	73.28	75.45
TiO <sub>2</sub>	0.07	0.07	0.07	0.10	0.10	0.06	0.08	0.09	0.10	0.09	0.08	0.07	0.11
Al <sub>2</sub> O <sub>3</sub>	11.51	11.50	11.85	11.97	12.06	12.09	12.19	12.53	11.83	12.45	12.01	12.39	12.83
FeO	0.53	0.57	0.57	0.59	0.64	0.61	0.59	0.64	0.58	0.56	0.64	0.57	0.81
MnO	0.08	0.08	0.07	0.07	0.10	0.06	0.10	0.09	0.10	0.09	0.07	0.10	0.10
MgO	0.09	0.09	0.07	0.11	0.12	0.11	0.13	0.09	0.09	0.10	0.09	0.10	0.12
CaO	0.61	0.57	0.63	0.61	0.62	0.62	0.64	0.59	0.63	0.62	0.62	0.60	0.67
Na <sub>2</sub> O	3.52	3.40	3.54	3.56	3.76	3.71	3.84	3.85	3.75	3.72	3.72	3.65	4.02
K <sub>2</sub> O	4.23	4.15	4.24	4.13	4.26	4.21	4.33	4.35	4.36	4.28	4.17	4.24	4.41
Total	90.11	90.36	92.46	91.73	94.96	93.69	95.78	96.17	94.24	96.18	93.85	95.02	98.51
<b>Stdev (1σ)</b>													
SiO <sub>2</sub> (wt%)	0.45	0.38	0.43	0.58	0.20	0.42	0.51	1.01	0.87	0.89	0.47	0.32	
TiO <sub>2</sub>	0.03	0.04	0.03	0.03	0.03	0.04	0.04	0.02	0.04	0.04	0.03	0.03	
Al <sub>2</sub> O <sub>3</sub>	0.34	0.23	0.32	0.10	0.36	0.09	0.12	0.18	0.39	0.24	0.21	0.22	
FeO	0.11	0.10	0.09	0.07	0.07	0.08	0.09	0.07	0.04	0.05	0.07	0.07	
MnO	0.05	0.04	0.04	0.05	0.03	0.06	0.06	0.03	0.05	0.04	0.03	0.05	
MgO	0.03	0.03	0.04	0.03	0.03	0.02	0.04	0.03	0.03	0.02	0.04	0.02	
CaO	0.03	0.02	0.02	0.02	0.02	0.02	0.02	0.03	0.02	0.05	0.03	0.03	
Na <sub>2</sub> O	0.07	0.13	0.04	0.07	0.06	0.18	0.08	0.11	0.06	0.10	0.07	0.09	
K <sub>2</sub> O	0.15	0.09	0.04	0.10	0.09	0.07	0.07	0.06	0.05	0.09	0.15	0.13	

<sup>a</sup> The values in parentheses represent the error from duplicate analysis and analytical uncertainty ( $2\sigma$ ).

<sup>b</sup> "S<sub>glass</sub>" and "Bulk S" represent sulfur content in glass measured by SIMS and bulk sulfur content in glass and crystal by EA, respectively.

<sup>c</sup> The sample used for decompression experiments, JR1+S-g1 (g1) or JR1+S-g2 (g2).



**TABLE 2.** Results of oxidation experiment

Line#	Position ( $\mu\text{m}$ )	$\text{Fe}^{3+}/\text{Fe}_{\text{total}}$
1	20	0.53
	70	0.53
	120	0.46
	170	0.25
2	10	0.54
	40	0.47
	70	0.47
	100	0.31
	130	0.20

Figure 1

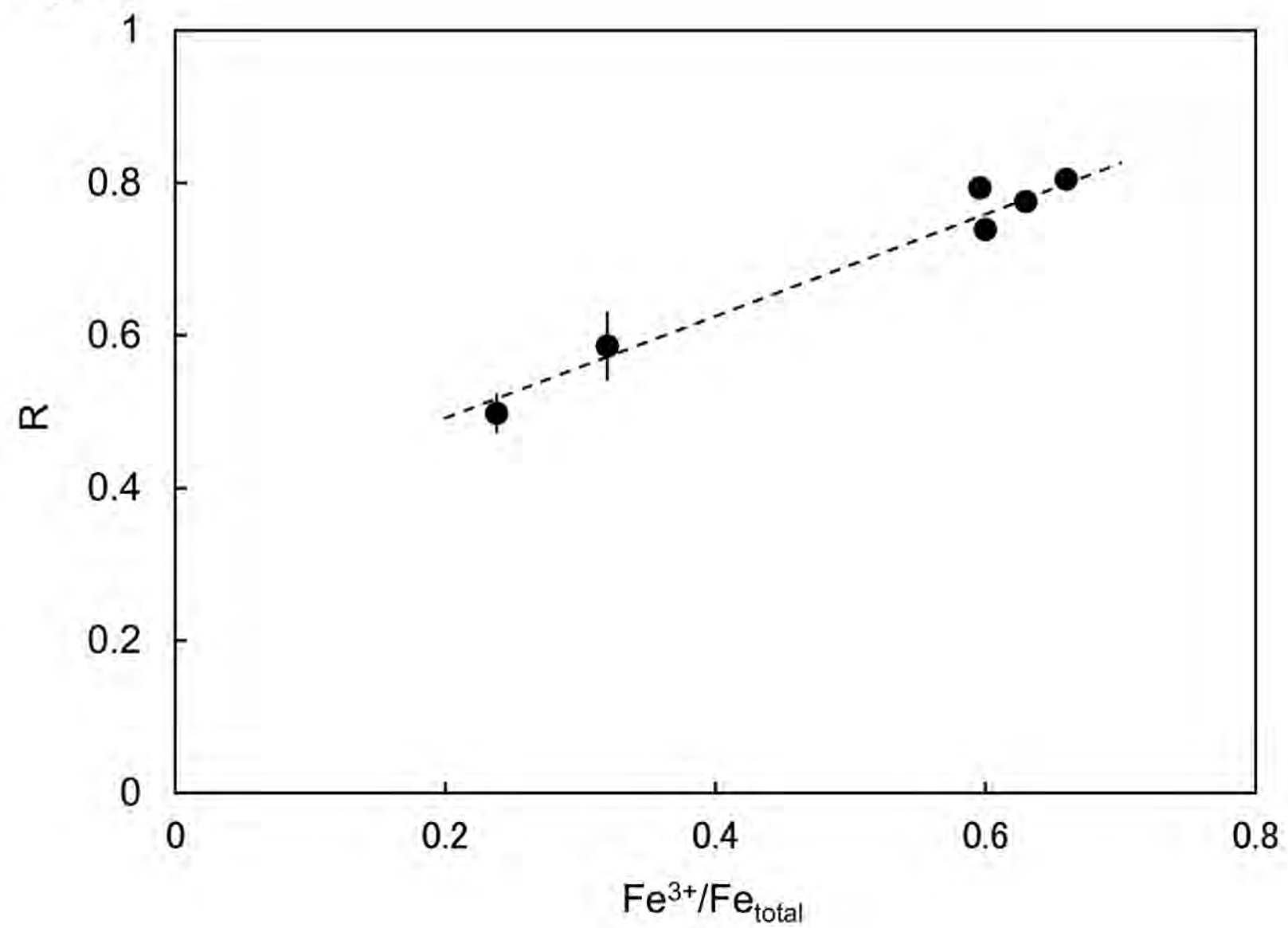


Figure 2

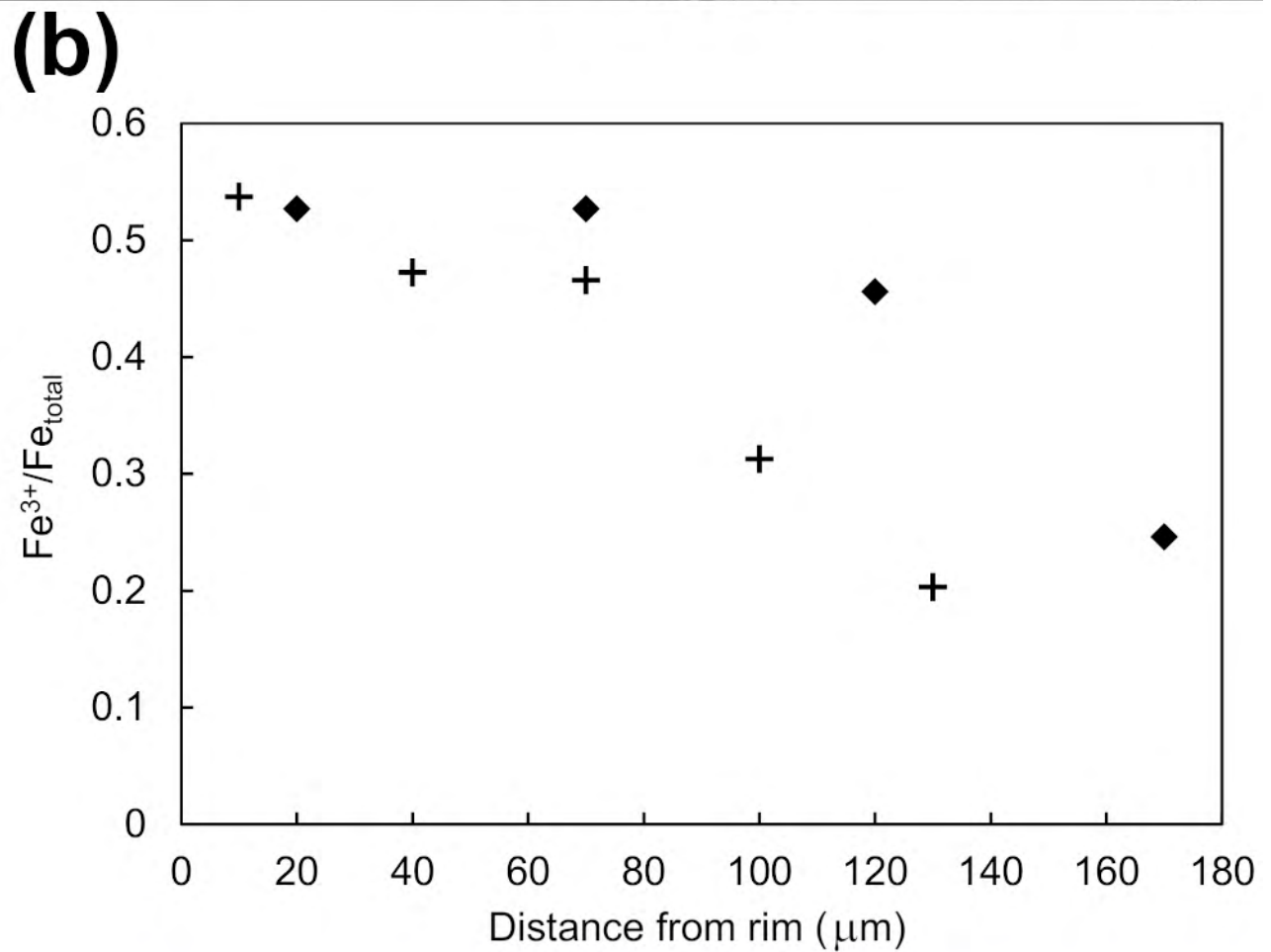
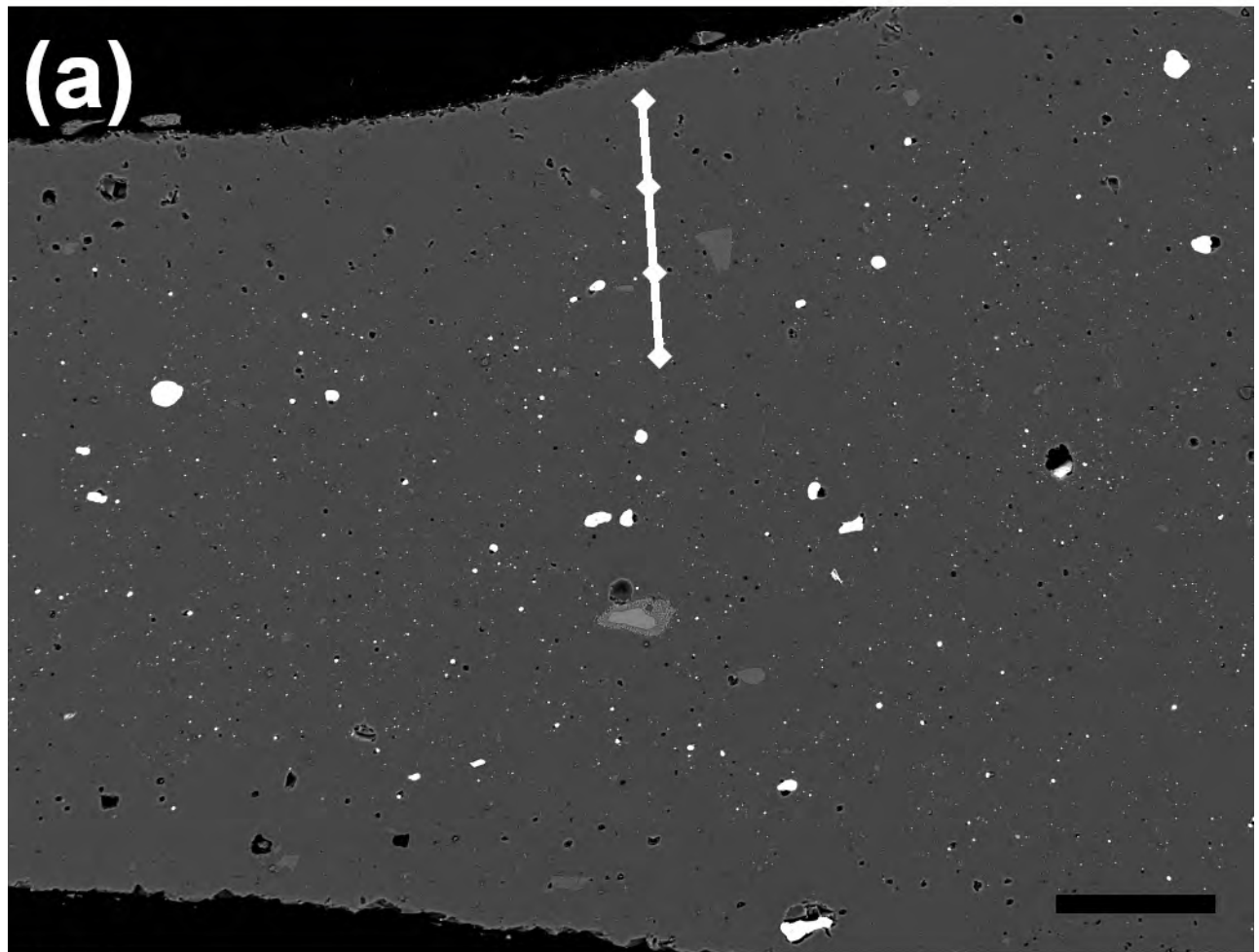
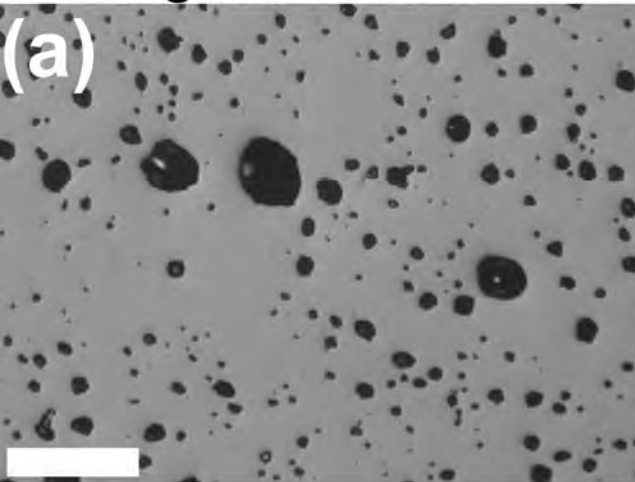
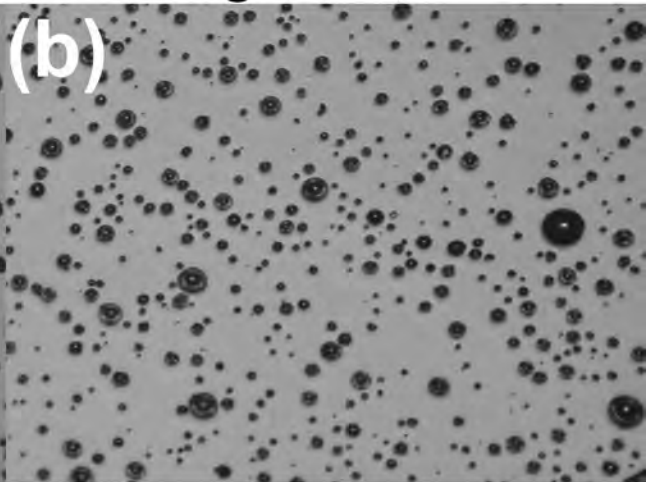


Figure 3

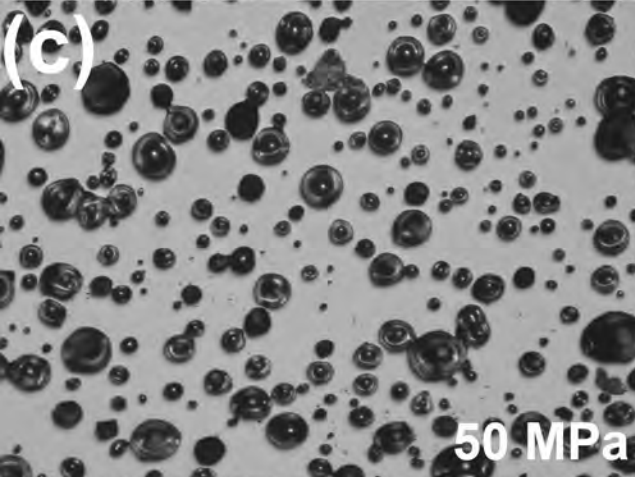
Starting material



Annealing



100 MPa/h



10 MPa/h

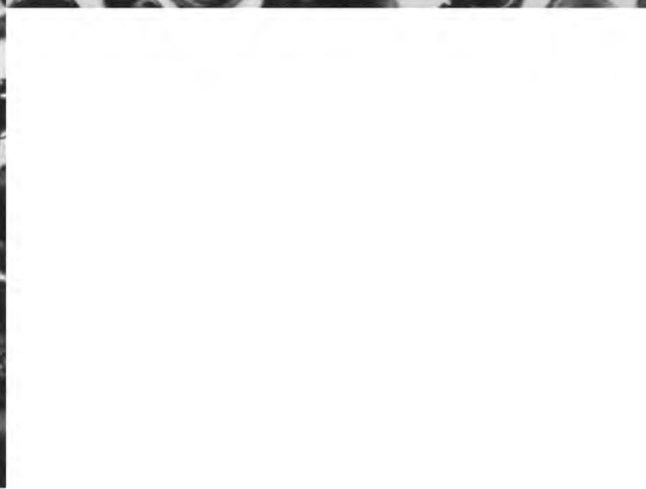
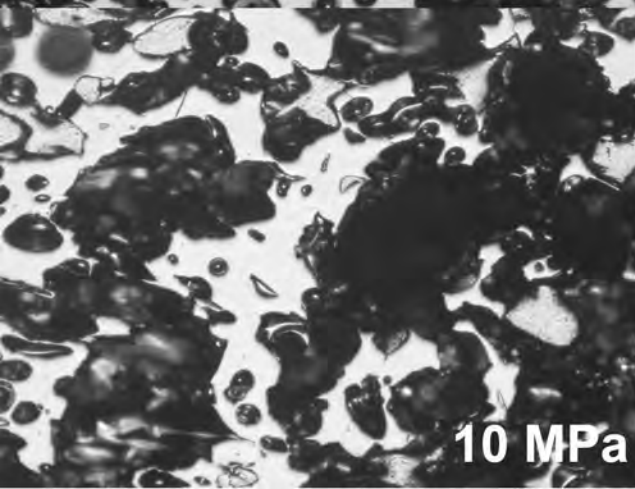
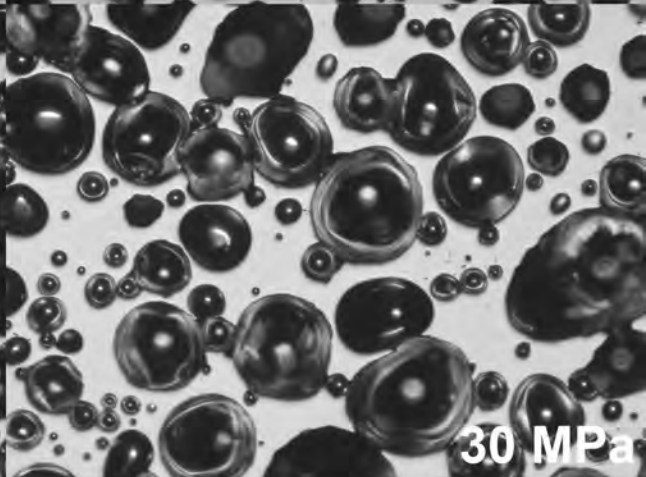
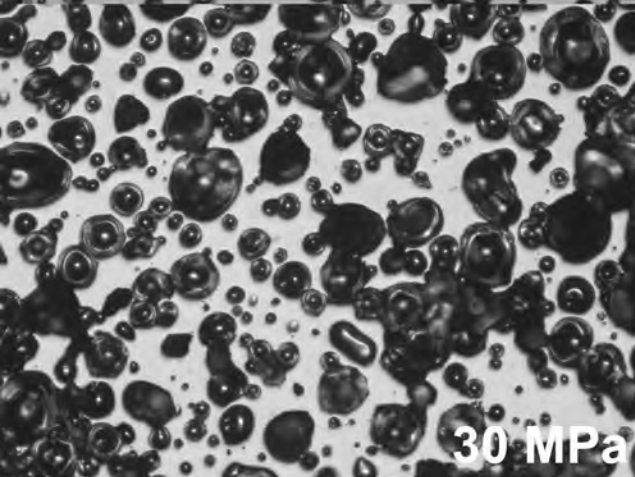
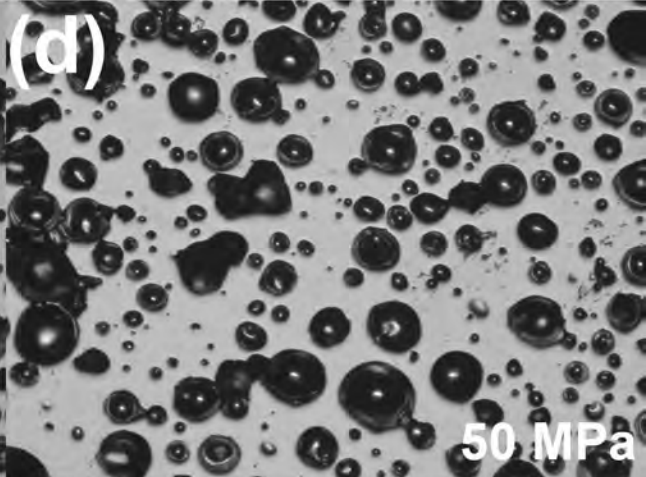


Figure 4

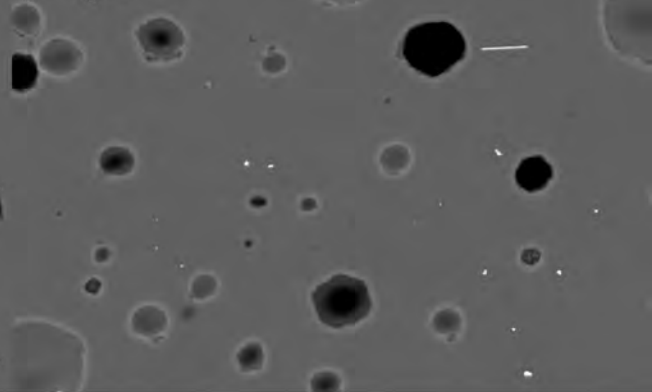
Starting material

(a)



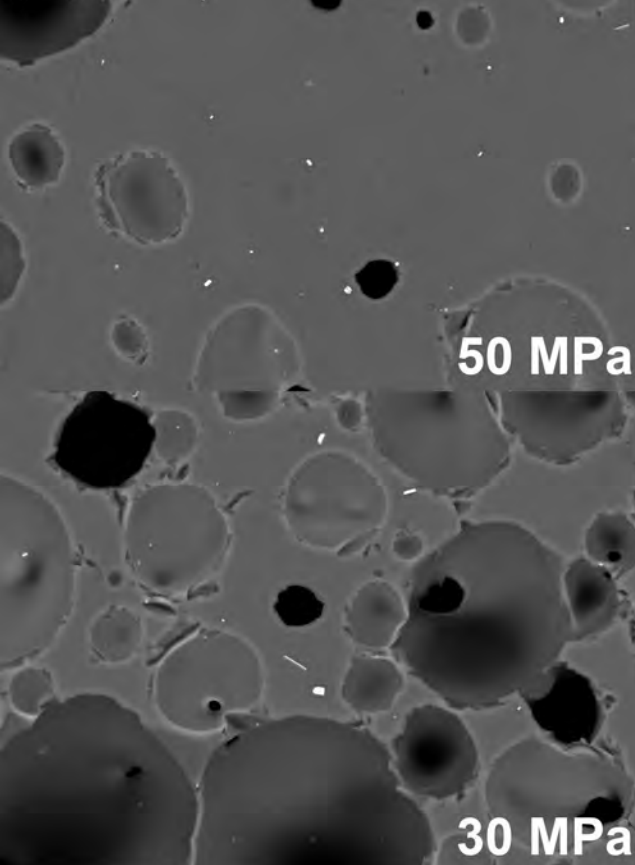
Annealing

(b)



100 MPa/h

(c)



10 MPa/h

(d)

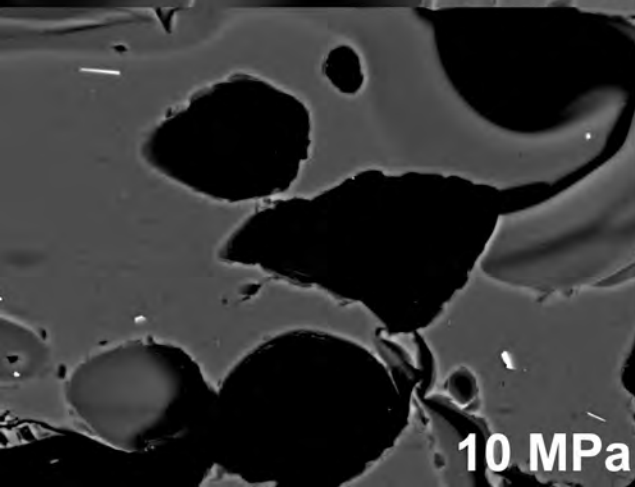
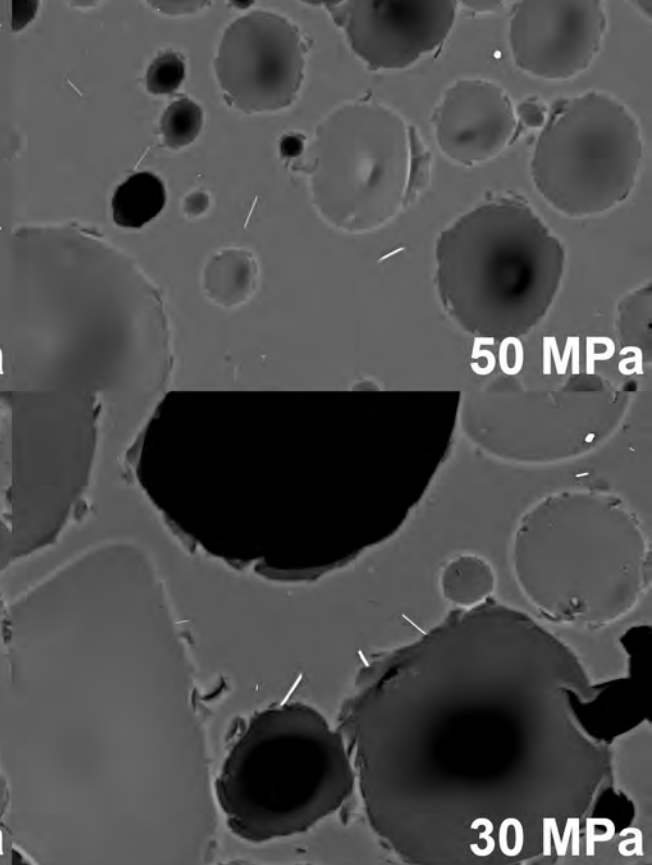


Figure 5

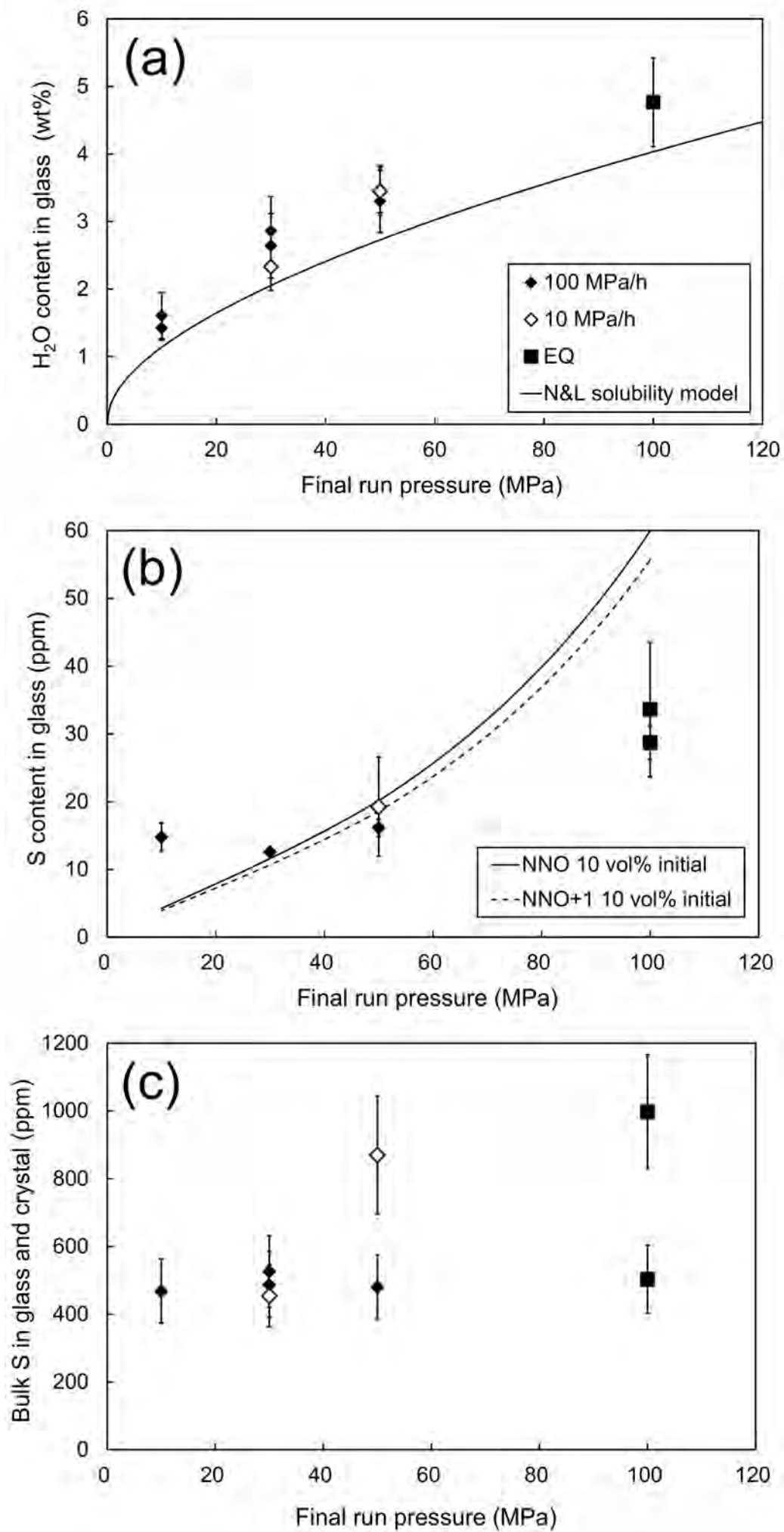


Figure 6

